Nuclear Engineering and Design 328 (2018) 121–133

Contents lists available at ScienceDirect

Nuclear Engineering and Design

journal homepage: www.elsevier.com/locate/nucengdes

Sensitivity and uncertainty analyses of ex-vessel molten core cooling in a flooded cavity during a severe accident

Byoungcheol Hwang[a], Kiyofumi Moriyama[a], Gisuk Hwang[b], Massoud Kaviany[c], Mooneon Lee[a], Eunho Kim[d], Hyun Sun Park[a,*]

[a] Division of Advanced Nuclear Engineering, POSTECH, Pohang, Gyeongbuk 37673, Republic of Korea
[b] Department of Mechanical Engineering, Wichita State University, Wichita, KS 67260, USA
[c] Department of Mechanical Engineering, University of Michigan, Ann Arbor, MI 48109, USA
[d] Korea Institute of Nuclear Safety, Daejeon 34142, Republic of Korea

ARTICLE INFO

Keywords:
Ex-vessel coolability
Debris particle bed
Particle agglomeration
Uncertainty analysis
Severe accident
Nuclear safety

ABSTRACT

Sensitivity and uncertainty analyses of molten core cooling under the ex-vessel phase of a severe accident of a light water reactor was performed with the COOLAP-I (COOLability Analysis Program-I) model, a parametric model considering one-dimensional heat transfer of a porous debris particle bed, covering a broad range of phenomena from the melt jet release to the long-term cooling process. COOLAP-I improved the previous version by including particle generation by the fuel-coolant interaction (FCI), and internal heat generation by the decay heat. With nine representative input parameters, an uncertainty analysis using Latin hypercube sampling (LHS) method with 300 samples were conducted, and the cooling characteristics such as total enthalpy, maximum temperature, decay heat ratio, and cake (a lump of connected particles) fraction, were examined for the elapsed time of up to 50 h. This analysis demonstrates the impacts of the water pool depth, the jet breakup-related parameters, and the accumulation area of the debris particles on the cake formation by particle agglomeration and analyzes the long-term coolability of debris particle bed in plant scale conditions.

1. Introduction

When a severe accident occurs in light water reactors (LWRs), the molten core slips down into the lower head of the reactor pressure vessel (RPV) (Sehgal, 2011). Since the relocated molten core has decay heat, it can penetrate the vessel and falls into the reactor cavity if the continuous adequate cooling of the molten core is not satisfied. The cooling of ex-vessel molten core is crucial for the mitigation and termination of severe accident progression within the containment, the last boundary for preventing the release of radioactive material to the environment. In some nuclear plants ones in Korea in particular, severe accident management (SAM) adopting the cavity flooding strategy inherently deals with complex thermal-hydraulic phenomena, such as the fuel–coolant interaction (FCI) before the molten-core concrete interaction (MCCI) during the ex-vessel phase (Park et al., 2001). In the FCI phenomenon, the melt jet penetrating RPV interacts with coolant water in the flooded cavity, and the breakup of jet occurs. If the length of melt jet breakup is longer than water pool depth, the melt in liquid phase directly relocates on the basemat concrete of the cavity. On the other hand, in case of the length of melt jet breakup much shorter than the water pool depth, the melt settles down on the cavity bottom with fully-fragmented particles. Although there are still uncertainties on vessel failure with the condition of melt discharge, the flooded cavity is one of the effective melt retention strategy for preventing the vessel failure.

Previous experimental studies related to the ex-vessel core melt coolability, however, showed the formation of particle agglomeration without the solidification of liquid melt. In corium-coolant mixing (CCM) tests using the COREXIT facility (Spencer et al., 1994), the re-agglomeration of particles was found by the limited quenching in the melt jet breakup phenomenon. The particle agglomeration with low porosity (0.3–0.4) was observed in the DEFOR experiments by Royal Institute of Technology (KTH) (Kudinov et al., 2010), which possibly hinders the cooling of the inner region in debris particle bed. In the FARO experiments using prototypical material (UO_2-ZrO_2 80:20 wt% mixture) (Magallon, 2006), an agglomerated lump was formed, even in the case the melt jet breakup length was shorter than the water pool depth. Above results indicate that the agglomerated lump of melt can be formed at the containment floor even under the condition of pre-flooding of the reactor cavity, and the agglomeration of the debris particles would adversely affect the cooling of the core debris.

* Corresponding author at: Department of Advanced Nuclear Engineering, POSTECH, Pohang 37673, Republic of Korea.
E-mail address: hejsunny@postech.ac.kr (H.S. Park).

https://doi.org/10.1016/j.nucengdes.2017.12.031
Received 10 April 2017; Received in revised form 12 December 2017; Accepted 20 December 2017

Nomenclature

V	volume, m^3
g	gravitational acceleration, m/s^2
A	surface or cross-sectional area, m^2
C	drag coefficient or jet breakup coefficient
L	melt jet breakup length, m
D	jet diameter, m
Δt_t	effective falling time of melt particle, s
$\Delta t_t'$	falling time without two-phase flow effect, s
d	particle diameter, m
c_p	specific heat, J/kg-K
T	temperature, K
t	time, s
k	thermal conductivity, W/m-K
r	radial coordinate or particle radius, m
q	heat flux, W/m^2
h	specific enthalpy, J/kg
Δh_{ex}	normalized excess specific enthalpy
Δh_{sl}	specific enthalpy of fusion, J/kg
<>	local volume average
P	operation power, MWth
F	cumulative mass fraction
d_e	absolute size constant
Bo_p	bond number
n	distribution constant
F_{sb},N_{sb}	subcool factors
Δz	thickness of loose particle bed, m

Greek symbol

α	thermal diffusivity, m^2/s
β	normalized time for the effective particle falling time
γ	fitting parameter for the effective particle transit time, m^{-1}
ρ	density, kg/m^3
σ	surface tension, N/m

Subscript

p	melt particle
D	drag
l	liquid (water)
v	vapor
fb	film boiling
r	radiation
sl	solid-liquid or fusion
s	solid phase or shutdown
0	infinite period before shutdown
MM	mass mean
sub	subcooled
lg	liquid-gas
eff	effective
DHF	dryout heat flux

To understand the characteristic of particle agglomeration, the detail mechanism for agglomeration phenomenon is needed, and several relevant numerical and analytical approaches were performed. The agglomeration phenomenon was considered in an IKEJET/KEMIX simulation based on the FARO experiment (Pohlner et al., 2006), while there was no concrete suggestion to resolve the detail mechanism of particle agglomeration. Recently, Hwang et al. (Hwang et al., 2016) suggested an analytical approach on the particle agglomeration and developed an analytical model, COOLAP-0[1], considering the particle heat release during sedimentation and one-dimensional heat transfer for the particulate and agglomerated (cake) parts of a debris particle bed. Based on its brevity, it can be applied for a broad range of the phenomena from melt jet release to debris particle bed cooling process, and this model was tested with the FARO experimental data (Magallon, 2006). In that research, the calculated mass fraction of the cake and the temperature transient on the bottom plate surface agreed well with the experimental data. They suggested the liquid phase sintering is likely to be the mechanism of particle agglomeration forming the brittle solid known as a cake.

A limitation of the COOLAP-0 model is the lack of ex-vessel phenomenon such as fragmented particle size distribution, decay heat, debris particle bed heat removal mechanism and so forth. In addition, the existing models considered only individual phenomenon (Pohlner et al., 2006; Moriyama et al., 2016a; Bürger et al., 2006), which may not clearly explain the coupled thermal-hydraulic phenomena on coolability including the debris particle bed formation by sedimentation of melt particles produced by melt jet breakup, separation of the particulate and cake parts of the debris particle bed, and long term cooling of the debris particle bed with the decay heat.

In this study, the COOLAP-I model was developed to assess the long-term cooling of a debris particle bed in the plant scale, with emphasis on the thermal-hydraulic phenomenon, aiming at explaining the influences of various factors on the ex-vessel debris coolability and related uncertainties. The model covers the process from the melt release from the RPV to the cooling of the particulate and cake debris particle bed, and the MCCI phenomenon is not included. In order to identify the effect of particle agglomeration clearly, the fully-fragmented of melt jet was assumed in the calculation which is similar with the COOLAP-0 model. Some additional models were implemented, such as decay heat and particle size distribution models, to apply the COOLAP-I model into the plant scale condition. The geometrical condition was set by assuming the severe accident conditions in a APR1400 plant, a Korean advanced pressurized water reactor. One-at-a-time sensitivity tests for fifteen input parameters (nine initial/boundary condition parameters and six model parameters) were performed, and nine parameters which have rather large sensitivity were selected as the uncertainty variables. Uncertainty analysis using Latin hypercube sampling (LHS) was performed, and four output variables were picked up (total enthalpy, maximum temperature, decay heat ratio, and cake fraction). Also, the importance analysis of them were examined (Cohen et al., 2013), and finally the dominant parameters and phenomena were identified in respect to the ex-vessel coolability of molten core.

2. COOLAP-I model for plant scale

In order to examine sensitivity and uncertainty analysis using the COOLAP-I model, the model needs to include key thermal-hydraulic phenomena from the melt jet breakup leading to the long-term cooling period. In Section 2.1, a brief description of the COOLAP-0 model (Hwang et al., 2016) based on the FARO experimental data (Magallon, 2006) is included. Based on the original model, some additional models are implemented, such as decay heat and a general particle distribution model as given in Section 2.2.

[1] COOLAP originally stands for "COOLability Analysis with Parametric fuel–coolant interaction model." Due to the continuous development of the model, the initial model was renamed as COOLAP (COOLability Analysis Program) Version 0, or COOLAP-0. The improved version of the model described in the paper is called to "COOLAP Version I or COOLAP-I."

2.1. The COOLAP model (COOLAP-0)

The COOLAP-0 model was developed for analyzing the characteristics of a debris particle bed and its cooling, and the target was the FARO experiment (Magallon, 2006). Key approaches related to the current study were repeated with the aid of the detailed description written by Hwang et al. (2016). The model was able to cover the whole time range of the process, from particle falling to debris particle bed cooling periods, as shown in Fig. 1 (Hwang et al., 2016), and was constructed with a simple approach. In the particle falling period, the melt jet breaks up with the fragmented melt particles, and they cool down while falling down to the cavity bottom. The falling time of a melt particle depends on the particle diameter, and is calculated by the balance among gravity, buoyancy, and drag forces as follows:

$$\rho_p g V_p - \rho_l g V_p + \frac{1}{2} C_D \rho_l A v_p = \rho_p V_p \frac{dv_p}{dt} \tag{1}$$

$$C_D = \max\left(24/Re_{d_p}, 18.5/Re_{d_p}^{0.6}, 0.44\right) \tag{2}$$

$$Re_{d_p} = \frac{\rho_v d_p v_p}{\mu_v}, \tag{3}$$

where ρ_p and V_p are the density and volume of the melt particle, g is the gravitational acceleration, ρ_l is the density of water, C_D is the drag coefficient, A is the cross-section of melt particle, v_p is the velocity of the melt particle, and t is the time, Re_{d_p} is the particle Reynolds number, ρ_v is the density of vapor, d_p is the particle diameter, and μ_v is the viscosity of vapor. The falling time for each size of melt particle is calculated, and the iteration method was used in the above ordinary differential equation with changing the velocity term into the first derivative of position ($v_p = dx/dt$). The melt jet breakup length was predicted by using the correlation of large size melt jet (Moriyama et al., 2005) as follows:

$$\frac{L_b}{D_J} = C_J \left(\frac{\rho_p}{\rho_l}\right)^{\frac{1}{2}}, \tag{4}$$

where L_b is the melt jet breakup length, D_J is the diameter of melt jet at the water surface, and C_J is a constant parameter (~10). The positions of melt particles produced by the breakup of melt jet differ from individual particles. However, it was assumed for brevity that all the produced particles were at the same height, somewhere within the jet breakup length from the water surface. Also, the only case that the melt jet is assumed to be fully-fragmented into particles before reaching the cavity bottom directly is considered. The influence of the fluid flow on the particle falling velocity was considered by comparing the theoretical terminal velocity from Eq. (1) and the velocity observed in the simulation of FARO experiments using JASMINE code by Moriyama and Park (2016). The correlation for falling time is as follows:

$$\Delta t_t = \beta \Delta t_t' \ (\text{for } \beta = 1 - e^{(-\gamma d_p)}), \tag{5}$$

where Δt_t is the effective falling time with the two-phase flow effect, β is the correction factor, and $\Delta t_t'$ is the falling time without the effect of two-phase flow. The correction factor (β) depends on the empirical parameter (γ) and particle diameter (d_p). The range of the particle diameter was 0.25–15 mm, based on the FARO experiment.

In thermodynamic consideration during the particle falling period, the temperature variation of each particle is calculated by using the transient heat conduction equation as follows (Kaviany, 2011):

$$\rho c_p \frac{\partial T}{\partial t} = \frac{k}{r^2}\left[\frac{\partial}{\partial r}\left(r^2 \frac{\partial T}{\partial r}\right)\right] + \dot{s}, \tag{6}$$

with the boundary conditions at the center region and outer surface given as (Kaviany, 2011; Poulikakos, 1994; Liu and Theofanous, 1995; Salikhov et al., 1999),

$$\frac{\partial T}{\partial t} = 3\alpha \frac{\partial^2 T}{\partial r^2} \ (\text{for } r = 0) \tag{7}$$

$$-k \frac{\partial T}{\partial t} = q_{fb} + \frac{7}{8} q_r \ (\text{for } r = r_p), \tag{8}$$

where c_p is the specific heat, T is the temperature, $\dot{s}$ is the liquid-solid phase-change thermal energy generation rate, k is the thermal conductivity, r is the radial position of melt particle, α is the thermal diffusivity, q_{fb} and q_r are the film boiling heat flux and the radiation heat flux, respectively, and r_p is the radius of the melt particle. In addition, the solidification near the interface was considered using the enthalpy method (Voller and Cross, 1981).

After the melt particle settles on the cavity bottom, the thermal state

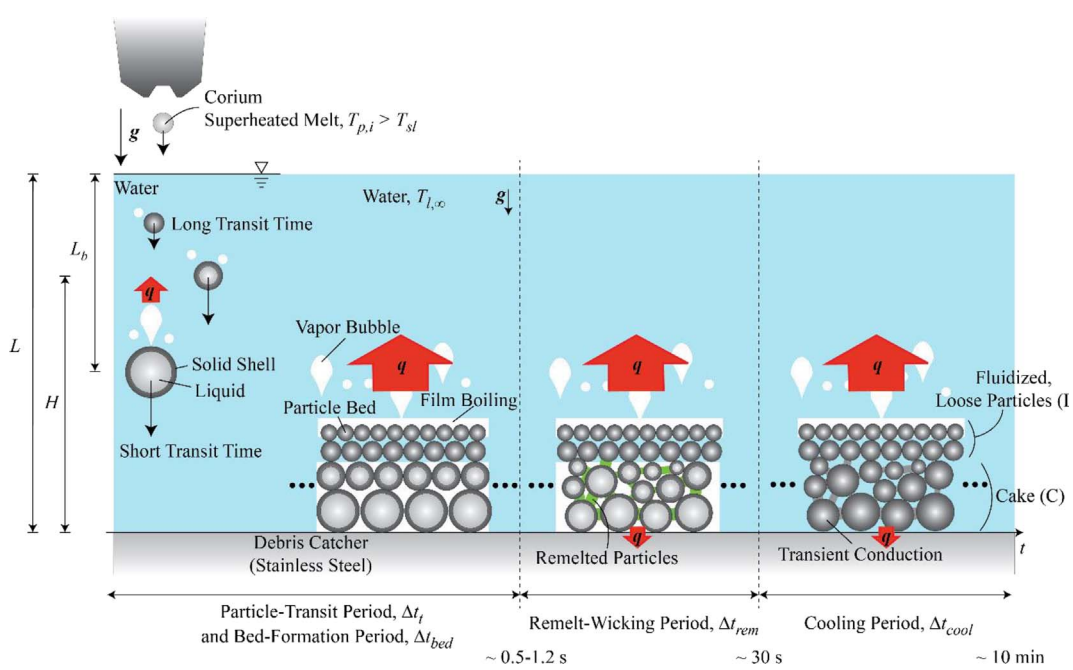

Fig. 1. Whole time process from melt jet breakup to long-term cooling in the scenario of ex-vessel severe accident (Hwang et al., 2016).

of the melt particle should be calculated because the melt particle can remelt when its enthalpy is larger than the enthalpy for phase change. In the COOLAP-0 model, when the particle arrives at the bottom, the criterion of solidification is determined by the excess specific enthalpy (Δh_{ex}) at the arrival time:

$$\Delta h_{ex} = \frac{\frac{1}{V}\int_V h dV}{c_p T_{sl} + \Delta h_{sl}}, \tag{9}$$

where V is the particle volume, h is the enthalpy of the particle, c_p is the specific heat, T_{sl} is the melting temperature, and Δh_{sl} is the heat of fusion. The thermoplastic properties of molten corium have been reported by Kim et al. (2017), including rectification with the molecular dynamic and analytical results. If the value is larger than unity, the particle re-melts, and the liquid smears into the gap between melt particles forming a cake, which is a lump of connected particles (Fig. 2). The prediction of cake mass produced by the proportional constant is based on the correlation between the cake mass and the remelted mass based on the FARO data.

In the debris particle bed cooling period, the heat transfer between the debris particle bed and water coolant is considered. The loose particle and cake are considered to be a fluidized particle and a fixed porous medium, respectively. Average thermophysical properties are assumed for each region, and the effective thermal conductivity, $<k_{eff}>$, of the cake region is represented by the summation of solid phase conduction, $<k_s>$, and radiation effects, $<k_r>$ (Kaviany, 2012). The heat transfer in the loose particle-water interface adopts the pool boiling correlation (Nukiyama, 1966) and the contact resistance between the cake region and bottom plate is considered to be a constant value (Schneider, 1985).

2.2. Modification for the plant scale analysis

In this research, the COOLAP-I model was improved in order to analyze the ex-vessel cooling phenomenon in plant scale. First, the geometric information, which was based on FARO experiments, was changed into plant scale for nuclear power plants, so APR1400 is considered as a reference plant. The corium property and various parameters such as melt jet diameter, initial jet velocity, and reactor cavity depth are shown in Table 1 (Annunziato et al., 1997; Park et al., 2011; Kim et al., 2005). Also, the material property of the cavity bottom for the plant scale condition was considered as siliceous concrete (Sevón (2005); Kodur, 2014), instead of the stainless steel debris catcher in the FARO case. Further details for the various parameters are described in Section 3.1.

In the cooling period of debris particle bed in the COOLAP-0 model, the porosity of the loose particle and cake is assumed to be 0.5 according to the FARO data (Magallon, 2006). However, the cake constructed by the liquid sintering process has a lower porosity than the loose particle bed about the volume of liquid soaking into the gaps. Therefore, an additional concept about the reduced porosity of cake (ε_{cake}) by the liquid sintering was considered as follows:

$$\varepsilon_{cake} = \varepsilon_{LP} - \frac{V_{remelt}}{V_{LP}}, \tag{10}$$

where ε_{LP} is the porosity of loose particle bed which is assumed to fixed value in this research, V_{remelt} is the volume of the remelt, and V_{LP} is the volume of the loose particle. The original model based on the FARO data needs not consider the decay heat, but the decay heat model should be implemented in the long-term cooling process, so the simple correlation of decay heat [$P(t_s)$] by ANS 2005 (fission products, ^{239}U and ^{239}Np) was implemented in this research as follows (Todreas and Kazimi, 2012):

$$\frac{P(t_s)}{P_0} = 0.1250 t_s^{-0.2752} \text{ (for } 10^2 \le t_s \le 10^6\text{s)}, \tag{11}$$

where P_0 is the operation power for an infinite period before shutdown (4200 MWth in this case), and t_s is the time after shutdown. Although the magnitude of decay heat in the initial period is larger than one in the long-term period, the effect of decay heat in the initial period is neglected by the dominant enthalpy of melt particle, and is rather dominant in the scenario of late-phase ex-vessel cooling.

The size of fragmented melt particles should be considered, because the thermal state in the debris particle bed depends on whether the melt particle remelts or not. In the FARO experiment, the particle size distribution was produced by the experimental results one by one. In this research, an empirical correlation for the size distribution proposed by Moriyama et al. (2005) was added. This correlation was produced based on various experiments such as FARO (Magallon, 2006) and PREMIX (Pohlner et al., 2006). The cumulative size distribution using the Rosin–Rammler distribution (Hinds, 2012) is shown as follows:

$$F = 1 - \exp\left[-\left(\frac{d_p}{d_e}\right)^n\right] \tag{12}$$

where

$$d_e = \frac{d_{MM}}{C_{dist}(\log_{10}2)^{1/n}}, \; n = 1.5 \tag{13}$$

$$d_{MM} = \left(\frac{\mathrm{Bo}_p \sigma_p}{\rho_p g}\right)^{1/2} \tag{14}$$

$$\mathrm{Bo}_p^{1/2} = F_{sb}\left(\frac{\rho_v}{\rho_l}\right)^{1/3}\left(\frac{\rho_l}{\rho_p}\right)^{2/3} \tag{15}$$

$$F_{sb} = 25\{2.2 - \exp(-13 N_{sb})\} \tag{16}$$

$$N_{sb} = c_{pl}\Delta T_{sub}/\Delta h_{lg}, \tag{17}$$

where F is the cumulative mass fraction of particles smaller than the diameter d_p, d_{MM} is the mass median diameter, d_e is the absolute size constant, and n is the distribution constant. The mass median diameter is calculated by using the Bond number (Bo_p), surface tension of melt particles (σ_p), density of melt particles (ρ_p), and gravitational acceleration (g). The Bond number is a function of subcool factors (F_{sb}, N_{sb})

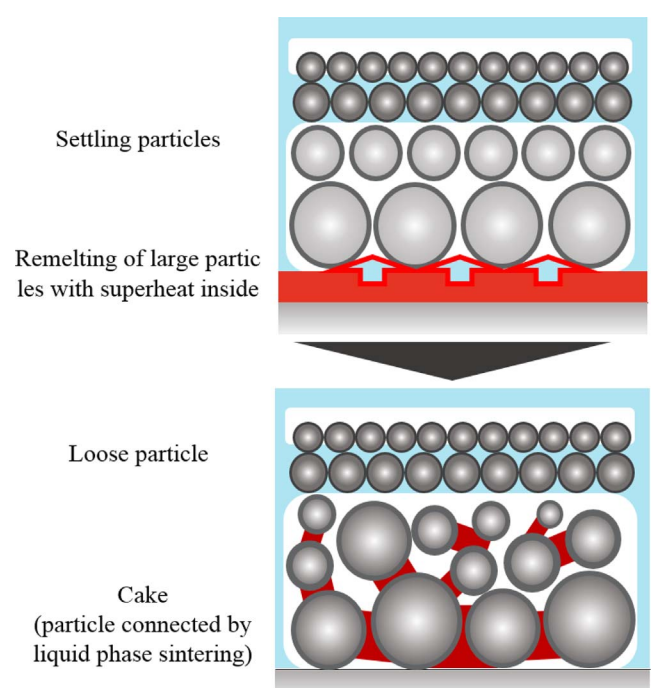

Fig. 2. Schematic diagram of cake formation by liquid phase sintering.

Table 1
Corium property and geometrical information for plant scale analysis.

Corium property (Annunziato et al., 1997)	
Melting temperature (K)	2840
Density (kg/m^3)	7960
Specific heat (J/kg-K)	565
Latent heat of fusion (MJ/kg)	0.362
Thermal conductivity (W/m-K)	2.88
Geometrical Information for APR1400 (Park et al., 2011; Kim et al., 2005)	
Diameter of the reactor pressure vessel (m)	5
Reactor cavity depth (m)	6.5
Area of cavity bottom (m^2)	84

based on the empirical approach. C_{dist} is the constant related to particle size distribution and its value is unity for the original size distribution model. This parameter is used as the input for sensitivity test in this research, so the range was determined based on experimental data mentioned above.

The heat transfer mechanism in the long-term cooling period is composed of conduction, convection, and radiation. In the COOLAP-0 model (Hwang et al., 2016), the effective thermal conductivity of loose particles was suggested to be 30 or 300 W/m-K based on heat pipe or fluidization modes of heat transfer. These two different values showed minor impact on the cooling rate of the debris particle bed in the simulation of FARO experiments. It was probably because the cooling of the relatively thin debris particle bed is dominated by heat transfer at the top surface (boiling), and the internal heat conduction resistance does not matter. For a plant scale debris particle bed, however, the overall heat transfer limitation should be more carefully considered. A reasonable approach should be the reference to the dryout heat flux (DHF), defined by the maximum heat removal rate from a porous medium divided by the area on the top, phenomenologically caused by two-phase counter-current flow limitation at the layer of loose particle bed (Cho et al., 1984). The effective thermal conductivity (k_{eff}) is evaluated from DHF (q_{DHF}) by the following relation:

$$q_{DHF} = k_{eff}\frac{\Delta T}{\Delta z}, \tag{18}$$

where Δz is the particulate debris particle bed thickness, and ΔT is the temperature difference through the particulate bed. The DHF was calculated using the Schmidt model (Schmidt, 2004). Lee et al. (2016) compared the model with available experimental data and evaluated the standard deviation of the data against the prediction. Considering the 2σ (95%) range, the DHF for the base case condition in this research was 8.35×10^5–1.874×10^6 W/m^2. This gave the range of effective thermal conductivity as 490–1100 W/m-K. The base case value was set 677 W/m-K. Note that the usage of DHF for heat transfer evaluation gives overestimated heat release rates for low temperature debris. In the present case, the debris temperature less than 1000 K is regarded cooled enough and no longer of interest, and this approach is reasonable.

Based on the models mentioned above, the COOLAP-I model was developed from the original model analyzing the particle agglomeration phenomenon in the FARO test to the modified model analyzing the coolability of ex-vessel molten core. This model covers from the particle falling period to long-term cooling of debris particle bed except for MCCI. For the connectivity among each period, the data of particle falling time is shared between particle falling period and debris particle bed formation period. Also, the data of thermal state is shared between debris particle bed formation period and long-term cooling period. The breakup of melt jet is assumed to fully-fragmented melt particle in the calculation in order to identify the effect of particle agglomeration in plant scale condition clearly. The input/output parameters for sensitivity tests and uncertainty analysis were selected, and the detailed information and ranges are described in Section 3.

3. Sensitivity tests and results

3.1. Input parameters and ranges

Table 2 shows the descriptions and ranges for fifteen input parameters for the sensitivity tests. It is composed of the initial/boundary condition parameters (Nos. 1–9) and the model parameters (Nos. 10–15) which are related to various phenomena such as melt jet breakup and cooling of debris particles. The table includes the range of parameters and the associated remarks, and the last column shows the sign of each parameter for brevity. Various input cases were determined by changing the specific value based on the condition of the base case (for example, in the case of high water temperature ('WTH' in Table 2), only the value of temperature was changed to 350 K with the other values remaining fixed). The base case values and variation width were given by referring to the previous uncertainty study on the ex-vessel melt jet breakup by Moriyama et al. (2016b) and the work on the COOLAP-0 model. The former considered existing severe accident analysis results for the melt jet and water pool conditions, and the latter gave the basis for some model parameter ranges. Note that the only scenario that the melt jet is fully-fragmented in the cavity bottom was considered in the particle falling period, so the range of some parameters such as jet dimeter, water depth is restricted by the condition of fully-fragmentation as shown in Table 2. Also, the concrete ablation or chemical reaction due to MCCI was not considered, and the heat transfer with fixed geometrical shape was applied for the temperature exceeding the concrete ablation (above 1500 K) in the long-term cooling period. Above basic assumptions were applied in both calculations of sensitivity test and uncertainty analysis.

3.2. Results for sensitivity tests

3.2.1. Particle falling period

Five parameters (jet diameter (JD), jet inlet velocity (JV), water depth (WD), jet breakup constant (CJB), and particle velocity constant (CV)) were considered in the particle falling period. In Table 2, the suffix 'H' represents the case using larger values (JDH, JVH, CJBH, and CVH) and 'L' represents the case using lower values (WDL1, WDL2, and CJBL) in the range.

The calculation results of the particle falling time according to particle size are shown in Fig. 3. The curve in the graph changes drastically near the 0.006 m region because of the flow transition regime due to the change of drag coefficient which is the function of particle Reynold number (in Eqs. (2) and (3)). As the particle size becomes larger, the falling time becomes decreases due to the reduction of drag. The large particle velocity constant (CVH) case shows a small deviation from the base case, and is very close to the base case when the particle size becomes larger because the large particle is less disturbed. Test cases of the jet breakup constants (CJBH, CJBL), large jet diameter (JDH), and two shallow water pool depths (WDL1, WDL2) show a large difference with base case in large particle region which has a high probability to form remelt liquid state. The above results show that the falling time is sensitive to jet breakup constant, jet diameter, and water pool depth, which affects the traveling length of a melt particle.

3.2.2. Debris particle bed formation period

For the debris particle bed formation period, the results of normalized excess specific enthalpy (Δh_{ex}) and cake fraction were calculated using three additional parameters (water temperature (WT), initial melt temperature (MT), and view factor (VF)). The normalized excess specific enthalpy was defined for the criteria of particle remelts, as mentioned in Section 2.1, and Fig. 4 shows the graph of thirteen input conditions, including the base case. For the quantitative analysis of these results, the differences between the base case and other input conditions for the 5 mm and 10 mm particle region were calculated and the results are shown as a bar graph (Fig. 5(a) and (b)). The test cases of

Table 2
Description and ranges for fifteen input parameters for sensitivity test.

No.	Parameter	Range	Remarks	Basecase	Cases		Sign
1	Water temperature [K]	300–350 (300, 350)	The range is based on various accident sequences, e.g. Loss Of Feed Water (LOFW), Small Break Loss Of Coolant Accident (SBLOCA), Middle Break Loss Of Coolant Accident (MBLOCA), Loss Of Offsite Power (LOOP), Station Black Out (SBO), and Total Loss Of Feed Water (TLOFW) (Park et al., 2011; Ahn et al., 2012)	300	–	WTH	WT
2	Jet diameter* [m]	0.2–0.28 (0.2, 0.28)	The main cause of vessel fracture is the failure of In-Core Instrument tube (~0.076 m diameter hole) (Sairanen et al., 2007), so the multi-failure of ICI tube was considered. Note that the calculation of the jet diameter at the water surface considers the free fall acceleration and jet shrinking phenomenon	0.2	–	JDH	JD
3	Jet velocity [m/s]	6–12 (6, 12)	The range is calculated based on the 1 MPa, and maximum mass of melt liquid (Moriyama et al., 2016a), and the value of basecase is set to 6 m/s	6	–	JVH	JV
4	Water depth* [m]	3.5–5 (3.5, 4.5, 5)	The effect of water pool depth is important because it can cause steam explosion according to the variation of pool depth (Moriyama et al., 2016a)	5	WDL1 (4.5) WDL2 (3.5)	–	WD
5	Melt initial temperature [K]	2900–3400	The range is based on the scenario of low pressure sequence in the severe accident (Sairanen et al., 2007)	3150	MTL	MTH	MT
6	Melt mass [t]	120–145 (120, 145)	The total mass of melt. The amount of melt was examined based on various accident sequences (Ahn et al., 2012; Rempe and Lead, 2005)	145	MML	–	MM
7	Porosity	0.3–0.6	The porosity determines the flow characteristics of coolant in the inner structure of bed, so it can affect the coolability in long-term period. The range of porosity is based on experimental results (Dinh et al., 2008), and the median value was selected for basecase	0.45	POL	POH	PO
8	Accumulation area [m^2]	21–84	In SECY-93–087 (USNRC, 1993), the minimum required value, the ratio of cavity floor area to thermal power of reactor, gives 0.02 m^2/MWth. In ARP1400, the total area of cavity floor is 84 m^2, so the half value was selected for basecase	42	AAL	AAH	AA
9	Duration after shutdown [h]	2–20 (2, 20)	The reduction rate of decay heat power is drastic according to time variation, and this can affect the coolability of debris particle bed. The range from 2 to 20 h was determined in this research	2	–	TAUH	TAU
10	Effective thermal conductivity [W/m-K]	490–1100	The range of effective thermal conductivity 490–1100 W/m-K. The base case value was set 677 W/m-K (detailed description is shown in Section 2.2)	677	KLPL	KLPH	KLP
11	Jet breakup constant	0.5–0.9	This parameter controls the representative height along the melt jet, where melt particles falls down from, so the length of particle traveling is changed. The half of the melt jet (~0.5) was selected in basecase	0.7	CJBL	CJBH	CJB
12	Particle velocity constant	172.3–220.6	The falling time of fragmented melt particles is affected by the upward two-phase flow induced by the vapor generation, as considered by Eq. (5). This parameter corresponds to the constant γ, and the range given in the original model was used (Hwang et al., 2016)	172.3	–	CVH	CV
13	View factor	0.1–0.5	The radiation heat transfer is dominant in the initial cooling of melt particle because of very high temperature, so this factor has the representative meaning of heat transfer in the initial state (Hwang et al., 2016)	0.3	VFL	VFH	VF
14	Sintering effect constant	5–20	It affects the correlation between the mass of cake and that of remelted liquid. The range of parameter was based on FARO cases with the consideration of view factor (Hwang et al., 2016)	12	CSL	CSH	CS
15	Particle Size Constant	1.428–0.572	Based on the research of Moriyama et al. (Moriyama et al., 2005), the range is about 0.57–1.43 (Detailed description is shown in Section 2.2 with Eq. (13))	1	CDL	CDH	CD

* The parameter ranges of jet diameter, and water depth are restricted by the condition of fully-fragmented melt jet condition.

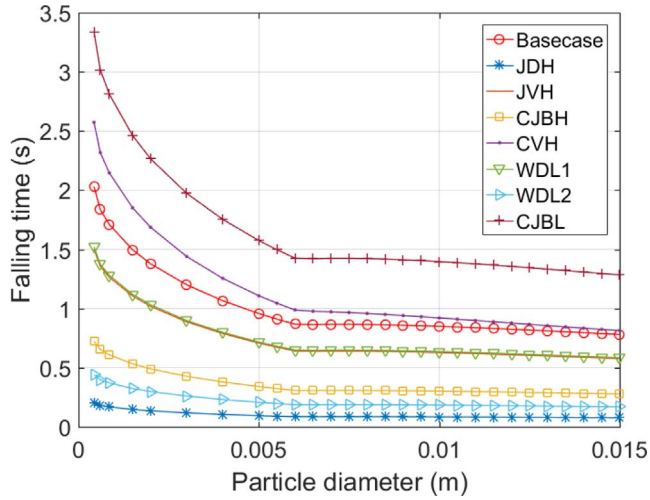

Fig. 3. Falling time of melt particle according to the particle size.

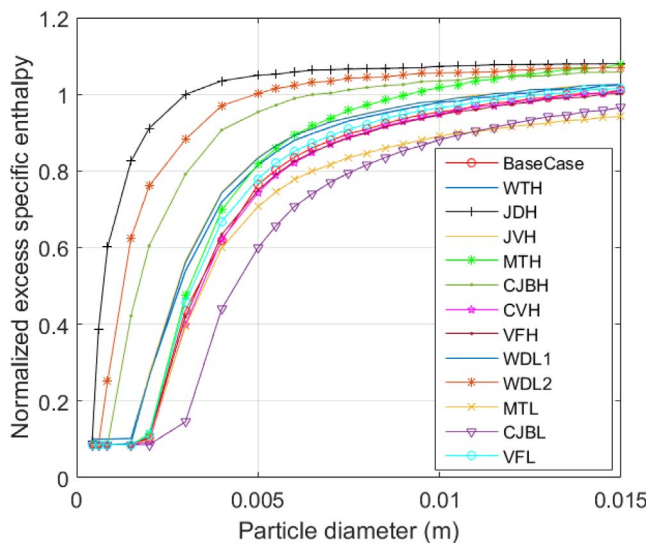

Fig. 4. Normalized excess specific enthalpy according to various input scenarios.

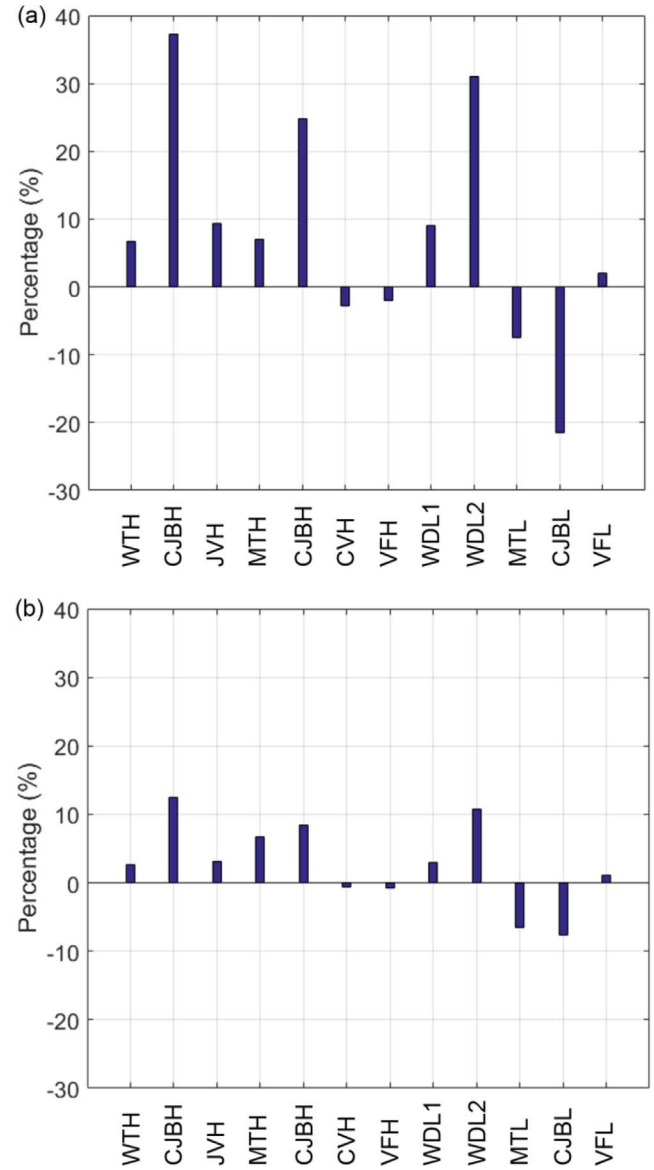

Fig. 5. The deviation from basecase for each input condition: (a) 5 mm particle region, and (b) 10 mm particle region.

large jet diameter (JDH), shallow water pool depth (WDL2), and jet breakup constant (CJBH, CJBL) show a large difference with base case in the bar graph. In addition, the impact of various input conditions becomes smaller according to the increase of particle size.

Fig. 6 shows the cake fraction, the ratio of the cakes mass to the total melt mass. Two more parameters (sintering effect constant (CS) and particle size constant (CD)) were considered in this calculation. The base case shows a very small cake fraction (~0.02), and three cases (JDH, CJBH, and WDL2) show that the whole part of the melt is cake. In addition, the test cases of high initial melt temperature (MTH) and large particle size constant (CDH) enable more chances to produce cake by the liquid sintering mechanism. However, test cases of the small particle constant (CDL), low initial melt temperature (MTL), and low jet breakup constant (CJBL) produced a particle bed formed with loose particles only.

3.2.3. Long-term cooling period

In the long-term cooling period, the calculation was performed after the debris particle bed was constructed. The end of the calculation was defined to be 50 h due to the computational limit. Fig. 7(a) shows the spatial distribution of temperature and (b) shows the history of temperature for the base case. In Fig. 7(a), the left region from the origin ($x < 0$ m) is the cavity bottom, and the thin high temperature (~2800 K) region ($x > 0$ m) is the cake, and the right of it is the loose particle. The initial temperature profile has discontinuity at the interfaces of concrete floor, cake and particle bed because the initial states of them are homogeneously given by the energy conservation law for each of the three parts. At the end of the calculation, the maximum temperature appears in the lowest part of the cake because of very low thermal conductivity in the cake and the concrete region.

The results for the long-term cooling period include maximum temperature, total enthalpy of the debris particle bed, and the decay heat fraction at the end of calculation. The results for maximum temperature and total enthalpy are shown in Figs. 8 and 9. Fig. 8 shows the results of initial/boundary condition parameters and model parameters. For the initial/boundary condition parameters, the test cases of large jet diameter (JDH), high initial melt temperature (MTH), and shallow water pool depth (WDL2) show a very high maximum temperature, which is larger than the concrete ablation temperature. In addition, the high melt jet velocity (JVH), and less shallow water pool depth (WDL1) cases show a rather high maximum temperature. In the case of model parameters, the test cases of the large jet breakup constant (CJBH), and the large particle size constant (CDH) show a very high maximum

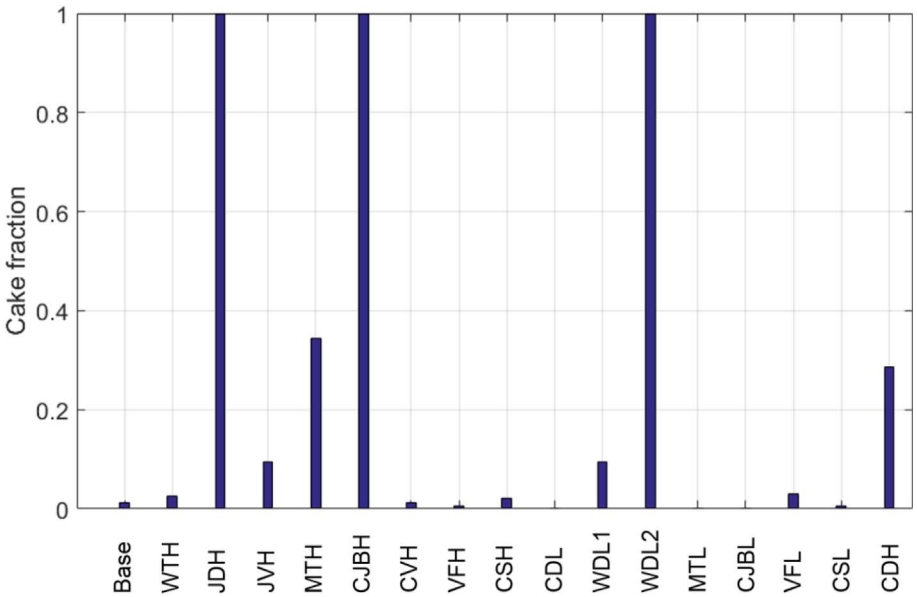

Fig. 6. The results of cake fraction according to various input conditions.

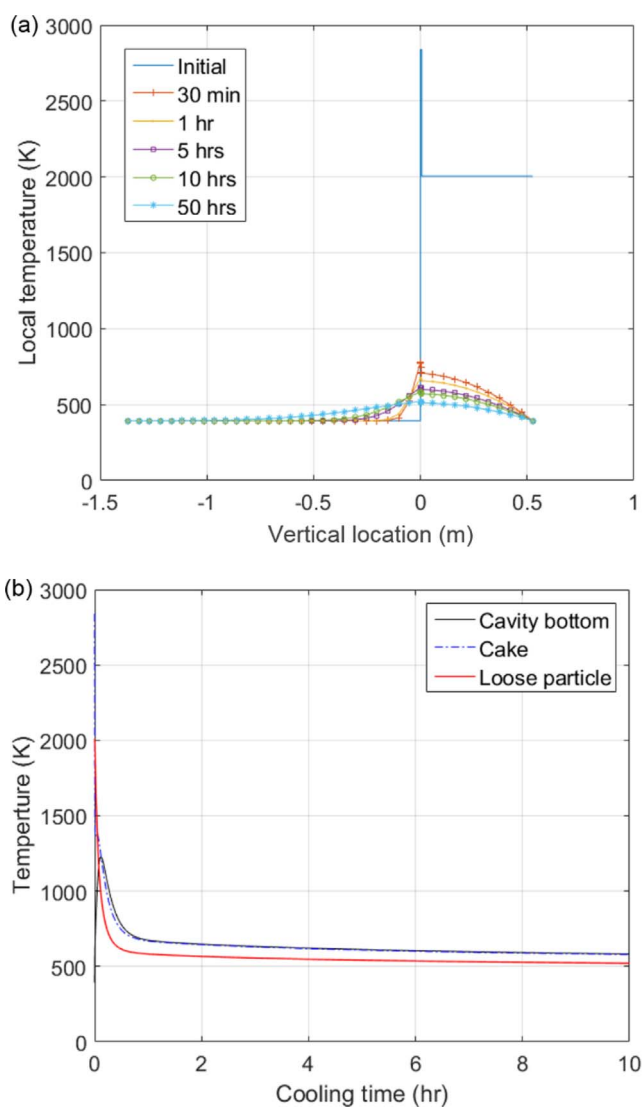

Fig. 7. (a) The spatial distribution of temperature, and (b) time history of temperature for basecase.

temperature. Other input cases that have no cake or very thin cake show a relatively low temperature near the minimum film boiling temperature (approximately 499 K). The trend of total enthalpy is nearly the same as that of maximum temperature (Fig. 9), which means that the lowest part of the debris particle bed is a dominant factor for analyzing the thermal state in the long-term cooling period.

Fig. 10 shows the impact of input variables on the decay heat fraction, which is defined by the ratio of decay heat to the heat removal at the top/bottom surfaces. The value should asymptotically approach unity when the initial enthalpy by the high temperature is mostly released. The internal heat generation by the decay heat balances with the heat release from the debris particle bed through the top and bottom surfaces, to water and to concrete, respectively. This equilibrium state is reached after a long time, when the debris particle bed temperature is almost equilibrated with the surroundings. Values smaller than unity indicate that the heat release is larger than the decay heat and the debris temperature will continue to decrease. This happens in the early phase when the initial high temperature dominates the heat transfer, or even in the relatively late phase when the heat removal is effective, so the heat release significantly exceeds the decay heat. Most of the cases showed values between 0.8 and 1, which indicate the situation mentioned above. Larger values were seen in the cases with large melt jet diameter (JDH), high melt temperature (MTH), large jet breakup constant (CJBH), very shallow water depth (WDL2), and a small particle size constant (CDH). Those cases had a large fraction of cake that was assumed to have low effective thermal conductivity, and to release a very small heat transfer.

4. Uncertainty analysis and results

Sensitive input parameters can be classified through sensitivity tests, as mentioned on Section 3. In uncertainty analysis, nine parameters composed of five initial/boundary condition parameters (jet diameter (JD), jet velocity (JV), water depth (WD), initial melt temperature (MT), and accumulation area (AA)), and four model parameters (thermal conductivity for loose particle (KLP), jet breakup constant (CJB), sintering effect constant (CS), and particle size constant (CD)) were considered as input variables based on the results of sensitivity tests. Other six parameters were not included in the uncertainty analysis due to their minor impacts on the final results of the cooling states. In Section 4.1, a detailed description for input parameters is presented with the ranges. The uncertainty analysis is described in Section 4.2, and the importance analysis of the input parameters is

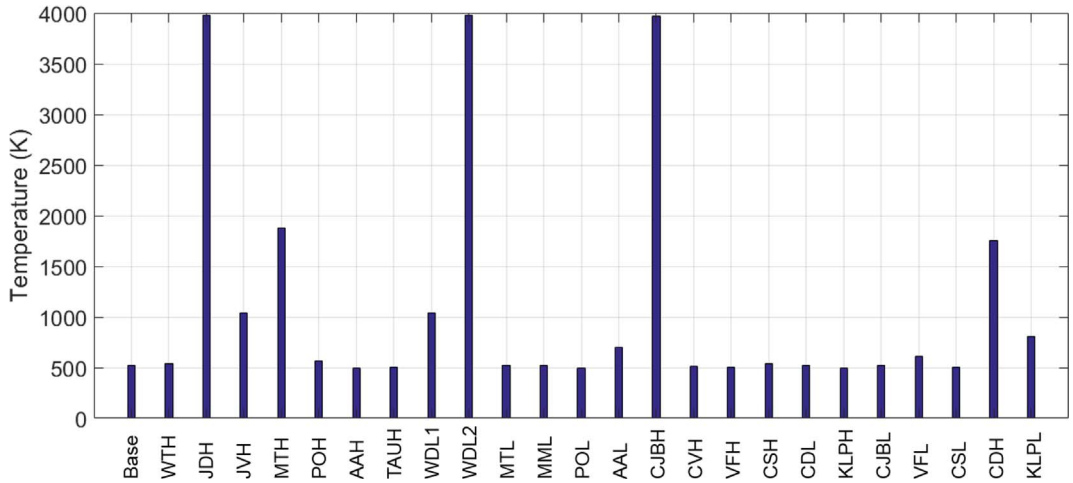

Fig. 8. The results of maximum temperature for various input conditions after 50 h calculation.

presented in Section 4.3.

4.1. Input parameters and ranges

Table 3 summarizes the uncertainty input variables, their ranges and distribution profiles. The input cases were generated by Latin hypercube sampling (LHS) with the given profiles. Based on the approach for applying probability distribution function (PDF) into input parameters (Moriyama et al., 2016b), the log-normal distribution which can handle rather large uncertainties compared to uniform distribution was used for the four input parameters (jet diameter (JD) and velocity (JV), initial melt temperature (MT), and particle size constant (CS)), so the range of values for the log-normal distribution was defined with the median (X_{50}) and the error factor, which is the ratio of the 95th or 5th percentile to the median. In case of the input parameter of jet diameter (JD) and jet velocity (JV), the upper value was applied due to the limitation of numerical approach in this research of which the height of melt jet does not exceed the water pool depth. The uniform distribution for the five other parameters (water depth (WD), accumulation area (AA), thermal conductivity of loose particulate (KLP), jet breakup constant (CJB), and sintering effect constant (CS)), and the assumption that the relation between input parameters is independent was applied in this research. In this kind of probabilistic approach, the results depend on the selection of input parameter range or distribution profile. Also, there are two types of uncertainties: the first one due to the deficient knowledge on phenomenological situation (model parameter), the second one due to the scenario-determined values (initial/boundary condition parameter), but the separation of such uncertainties is not considered for simplicity.

4.2. Results for uncertainty analysis

The calculation proceeded from the particle falling period to the long-term cooling period, and four kinds of output variables (total enthalpy (O1), maximum temperature (O2), decay heat fraction (O3), and cake faction (O4)) were determined. Input samples were generated by Latin Hypercube Sampling (LHS) (Khatib-Rahbar et al., 1989) based on Table 3. One set of test matrices contained 100 input samples, and three sets with 300 samples were analyzed.

The scatter plots for the four output variables against the nine input variables are shown in Fig. 11. The values of the total enthalpy (O1) and the maximum temperature (O2) of the debris particle bed mostly stayed at a lower level, indicating a well-cooled state, and a few cases show very high values. The majority of the cases showed the decay heat fraction (O3) close to 1, and zero or a very small fraction of the cake (O4). Some cases of hindered cooling showed large cake fractions. The

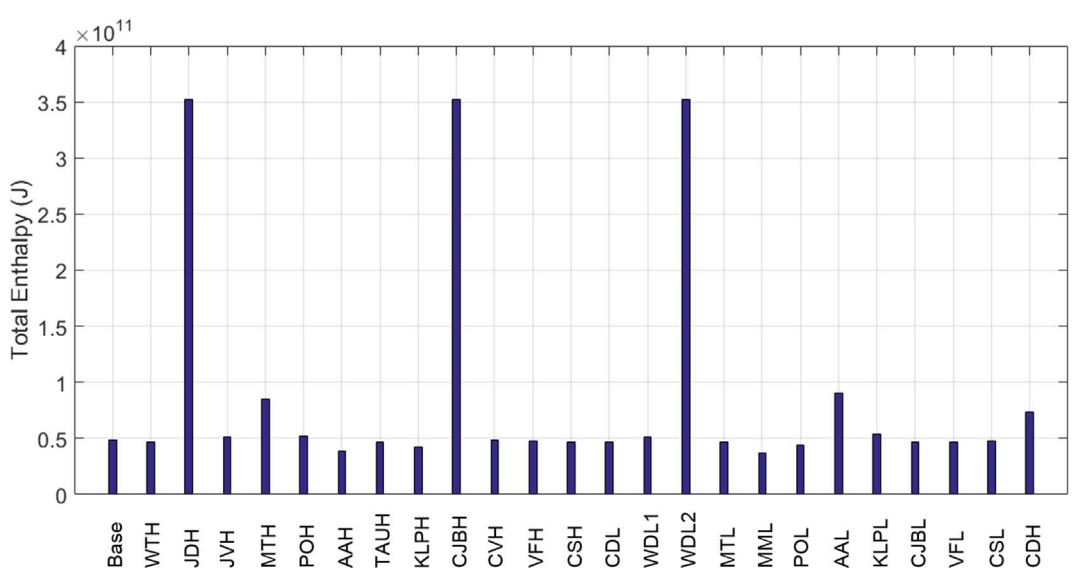

Fig. 9. The results of total enthalpy for various input conditions after 50 h calculation.

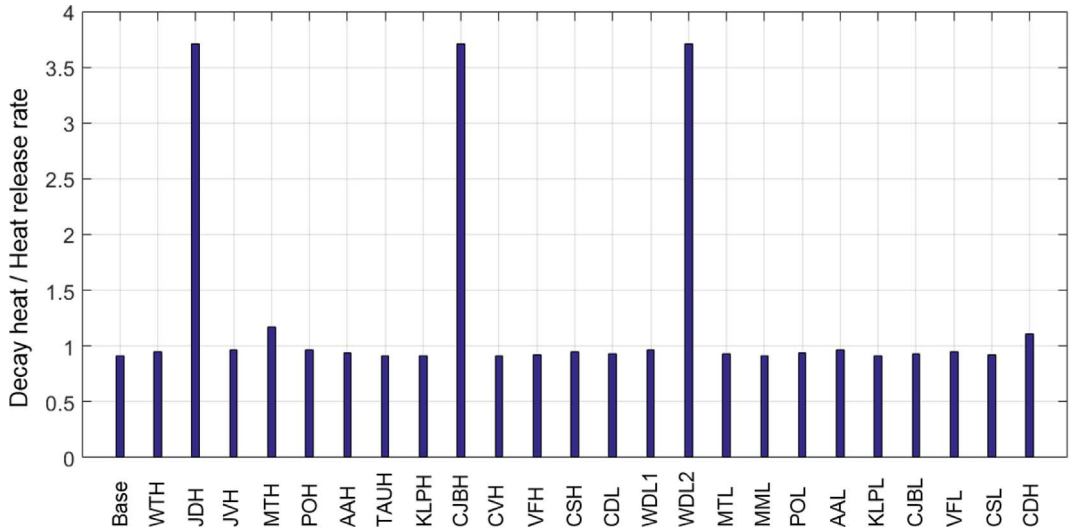

Fig. 10. The results of decay heat fraction for various input conditions after 50 h calculation.

Table 3
Uncertainty input parameters and their ranges.

Parameter	Description	Profile	Range	Sign
JD	Jet diameter (m)	Log-normal	X_{50} = 0.23, Error factor = 1.15	V1
JV	Jet velocity (m/s)	Log-normal	X_{50} = 8.4, Error factor = 1.4	V2
WD	Water depth (m)	Uniform	3.5–6.645	V3
MT	Initial melt temperature (K)	Log-normal	(Superheat) X_{50} = 170, Error factor = 2 (melting point ~ 2840 K)	V4
AA	Accumulation area (m^2)	Uniform	21–84	V5
KLP	Thermal conductivity of loose particle (W/m-K)	Uniform	490–1100	V6
CJB	Jet breakup constant	Uniform	0.3–0.7	V7
CS	Sintering constant	Uniform	5–20	V8
CD	Particle size constant	Log-normal	X_{50} = 1, Error factor = 1.5	V9

X_{50} = 50-th percentile; Error factor = $X_{95}/X_{50} = X_{50}/X_{05} = \sqrt{X_{95}/X_{05}}$.

cake fraction shows the separated trend of bottom and top ends due to the large value of the sintering effect (V8), the constant for proportionality of the remelt mass, and the cake mass. Among the input variables, the accumulation area (V5) shows a distinct trend, O1 and O2 decreased with increasing accumulation area (V5). Trends by other variables are not as clear.

In order to quantify the uncertainties for the four output variables, the cumulative distributions were examined as shown in Figs. 12 and 13. In these figures, the three green lines represent each set of 100 samples, and the pink line indicates the synthesis data which are the uncertainty analysis based on the whole three sets (300 input samples). In addition, the average, median, and 5th/95th percentile values for each set are shown in Table 4. In Fig. 12 (b), the probability of maximum temperature below 1200 K is about 85%, and a small fraction of cases shows a non-coolable state with a very high maximum temperature that is higher than the concrete ablation point (~1500 K) and the melting point of corium (~2800 K). For the decay heat fraction in Fig. 13(a), the probability of having a high temperature in the debris particle bed (which means larger than unity) is about 10%. In Fig. 13(b), the composition of the debris particle bed is likely to be loose particles by only an 80% probability, and whole parts of the debris particle bed becomes cake by an 8% probability.

4.3. Importance analysis

The relative importance of the input uncertainty variables in terms of the impacts on the outputs was examined by using the standardized regression coefficient (SRC), partial correlation coefficient (PCC), Pearson product moment correlation coefficient (PEC), and Spearman rank correlation coefficient (SPRC) (Cohen et al., 2013) as importance indices.

Fig. 14 shows the comparison of the importance indices for input variables V1–V9, in terms of every output variable, O1–O4. The accumulation area (V5) shows the most significant impact for total enthalpy (O1), maximum temperature (O2), and decay heat fraction (O3) by SPRC. The large values of rank correlation coefficients are due to the non-linearity caused by drastic jumps of the result variables, i.e. extremely high temperature with large fraction of cake. Other variables such as water depth (V3), jet breakup constant (V7), the jet diameter (V1) also show high importance. Considering that the jet breakup length is proportional to the jet diameter, three of the important factors, V1, V3, and V7 are all related to the geometrical aspect, the available length for the particle fall before settling on the floor. The cake fraction (O4) does not show any significant influence by the debris accumulation area (V5), and is most affected by V3 and V7, which is similar to the other result indices.

It was remarkable that the impact of the sintering constant (V8) is relatively weak even though the mass of the cake is calculated through multiplying the sintering constant by the remelted mass. This might be due to the change in the cake by other factors which are stronger, and the cake fraction is separated into two extreme values, nearly 0 or 1. Thus, the effect of sintering constant on the cake fraction mostly falls in insensitive zones. The effective thermal conductivity of the loose debris (V6) also shows only a weak influence. Those two variables, V8 and V6, are both quite uncertain model parameters from the mechanistic view point due to potentially complicated processes behind. So, weak impacts of them implies the usefulness of the present model in spite of its simplicity and crudeness.

5. Conclusions

The sensitivity and uncertainty of the long-term cooling of ex-vessel core debris were examined with the COOLAP-I model. The model covers melt particle sedimentation in a water pool, debris particle bed formation and the long-term cooling. For this research, it was modified to accommodate the geometrical condition assuming APR1400, and to include models for the particle size distribution and the decay heat.

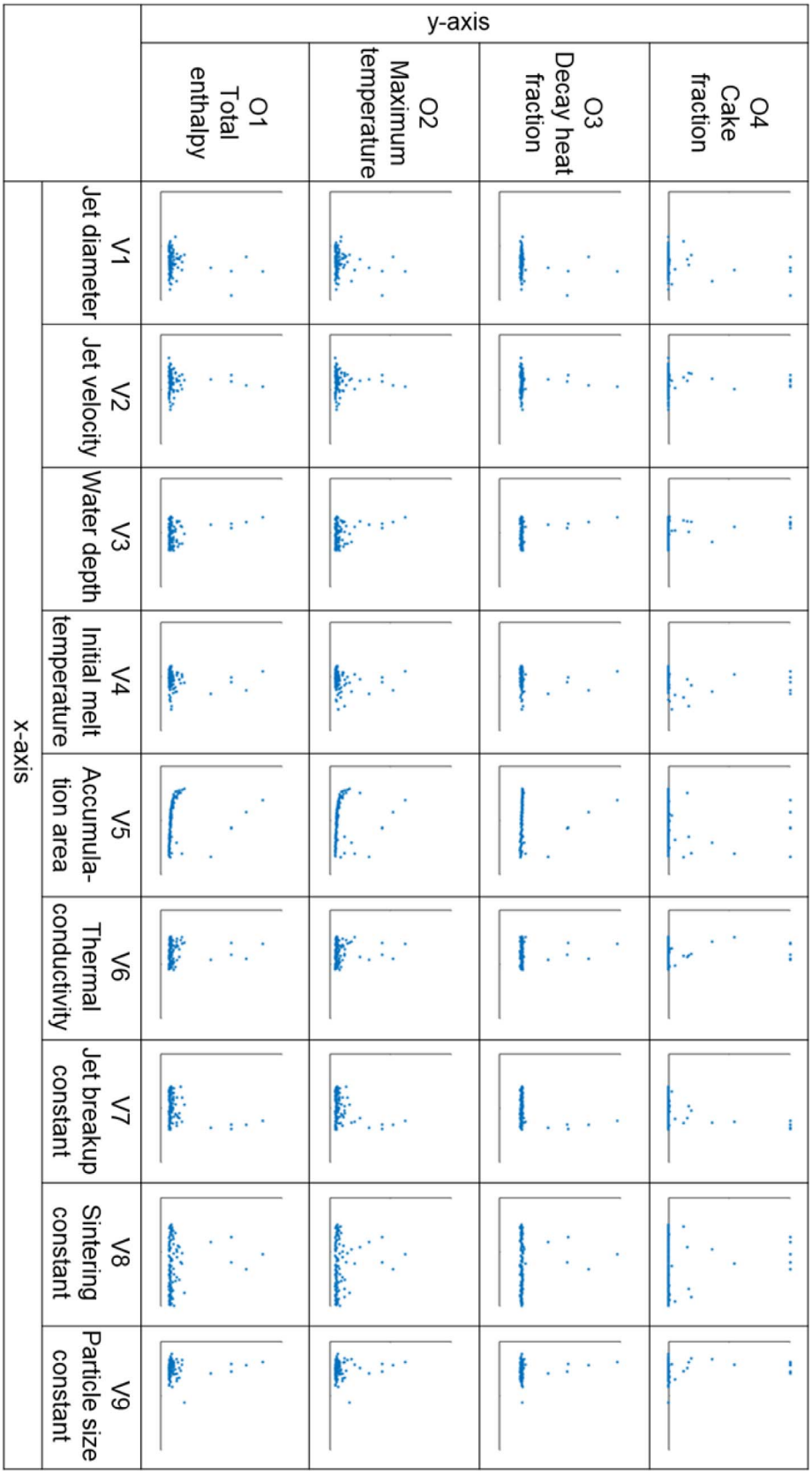

Fig. 11. Scattering plot of output variable (O1–O4) according to various input conditions (V1–V9).

Nine parameters, five for the initial/boundary conditions and four for the model, were selected as uncertainty variables through the sensitivity analysis, and impacts of their uncertainties were examined with four key output variables such as total enthalpy, maximum temperature, decay heat fraction, and cake fraction through LHS. The ranges of the input variable uncertainties were given by considering available severe accident analysis results, while partially limited due to the applicable range of the model (large fraction of the cake cannot be

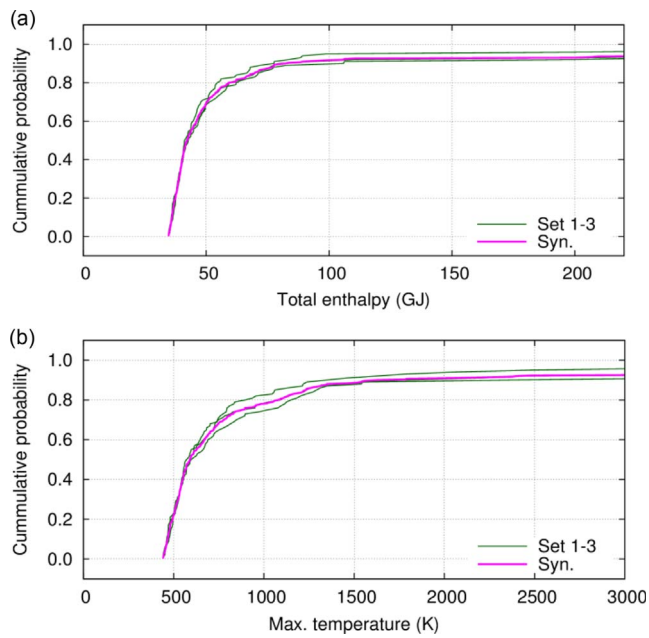

Fig. 12. The cumulative distributions of (a) total enthalpy and (b) maximum temperature.

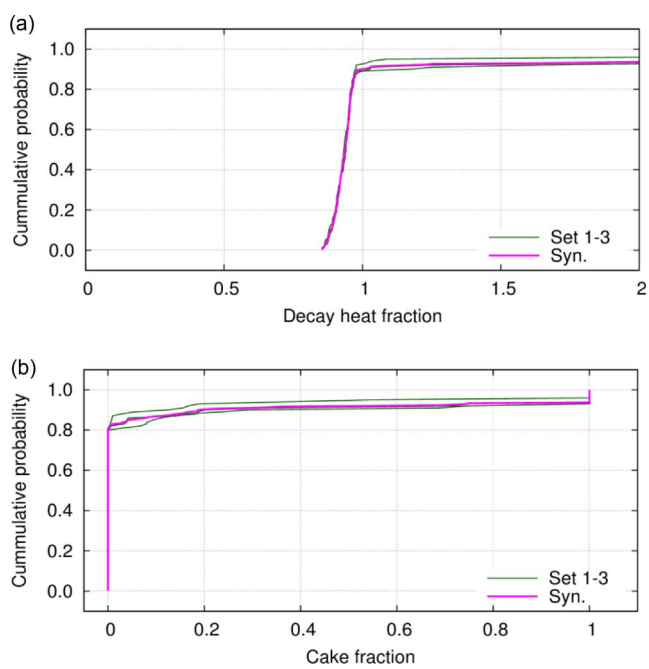

Fig. 13. The cumulative distributions of (a) decay heat fraction and (b) cake fraction.

treated and MCCI is not included). The results showed that the probability of debris particle bed cooling below 1200 K is 85%, the probabilities of totally loose particle bed formation and totally agglomerated cake formation are 80% and 8%, respectively. Note that these results are based on the simulation condition that the melt jet is fully-fragmented before reaching to the cavity bottom. The analysis of relative importance of input parameters showed that the accumulation area of debris particles, the water pool depth and the jet breakup length have strong influences on the cooling behavior. The cake fraction is dominated by the geometrical relation of the melt jet breakup length and the water depth, but not much affected by the debris accumulation area. The impact of the sintering effect constant, the given ratio of the cake mass to the liquid mass arriving on the floor, which is a quite uncertain model parameter, is unexpectedly weak. The effective thermal

Table 4
The average, median, and 5th, 95th percentile values of each output variable (O1–O4).

O1	Average	5th percentile	Median value	95th percentile
Set 1	6.73E+10	3.55E+10	4.27E+10	2.42E+11
Set 2	7.12E+10	3.51E+10	4.12E+10	2.67E+11
Set 3	5.99E+10	3.54E+10	4.21E+10	9.86E+10
Synthesis	6.61E+10	3.54E+10	4.22E+10	2.67E+11
O2				
Set 1	1.05E+03	4.56E+02	5.96E+02	3.96E+03
Set 2	1.08E+03	4.49E+02	5.71E+02	3.96E+03
Set 3	9.05E+02	4.55E+02	5.93E+02	2.48E+03
Synthesis	1.01E+03	4.55E+02	5.90E+02	3.96E+03
O3				
Set 1	1.10E+00	8.78E−01	9.41E−01	2.32E+00
Set 2	1.16E+00	8.72E−01	9.38E−01	2.49E+00
Set 3	1.05E+00	8.67E−01	9.33E−01	1.08E+00
Synthesis	1.10E+00	8.74E−01	9.37E−01	2.40E+00
O4				
Set 1	9.97E−02	0.00E+00	0.00E+00	1.00E+00
Set 2	1.04E−01	0.00E+00	0.00E+00	1.00E+00
Set 3	6.65E−02	0.00E+00	0.00E+00	5.41E−01
Synthesis	9.01E−02	0.00E+00	0.00E+00	1.00E+00

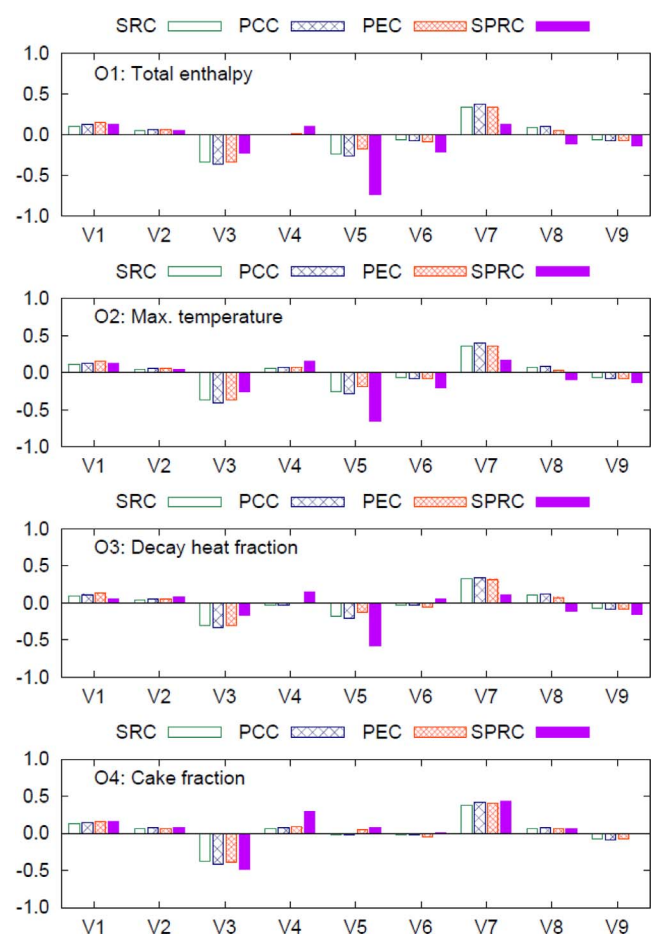

Fig. 14. The results of relative importance using standardized regression coefficient (SRC), partial correlation coefficient (PCC), Pearson product moment correlation coefficient (PEC), and Spearman rank correlation coefficient (SPRC).

conductivity of the loose debris also showed only a minor impact. The coverage and applicability of the current results are limited due to the model limitation, i.e. incomplete breakup of the melt jet in the water pool is not allowed, geometry and heat transfer of debris particle bed is very simply modeled. The model would be applicable for realistic accident conditions after improvement on such aspects, and be useful in

assessing the initial condition of MCCI in the cases the molten core is partially broken up in the coolant pool and under the cooling conditions such as the pre-flooded of the cavity in nuclear power plants as one of severe accident management strategies.

Acknowledgments

This work was supported by the Nuclear Safety Research Program through the Korea Foundation of Nuclear Safety (KOFONS), granted financial resource from the Nuclear Safety and Security Commission (NSSC), Republic of Korea (No. 1305008).

References

Ahn, K.I., Park, S.H., Kim, H.D., Park, H.S., 2012. The plant-specific uncertainty analysis for an ex-vessel steam explosion-induced pressure load using a TEXAS–SAUNA coupled system. Nucl. Eng. Des. 249, 400–412.
Annunziato, A., Addabbo, C., Yerkess, A., Silverii, R., Brewka, W., Leva, G., 1997. FARO Test L-14 on Fuel Coolant Interaction and Quenching. Comparison Report, Volume 1 + 2, Analysis of the Results (No. NEA-CSNI-R–1997-31). Organisation for Economic Co-Operation and Development-Nuclear Energy Agency.
Bürger, M., Buck, M., Schmidt, W., Widmann, W., 2006. Validation and application of the WABE code: investigations of constitutive laws and 2D effects on debris coolability. Nucl. Eng. Des. 236 (19), 2164–2188.
Cho, D.H., Armstrong II, D.R., Chan, S.H., 1984. On the pattern of water penetration into a hot particle bed. Nucl. Technol. 65 (1), 23–31.
Cohen, J., Cohen, P., West, S.G., Aiken, L.S., 2013. Applied Multiple Regression/Correlation Analysis for the Behavioral Sciences. Routledge.
Dinh, T.N., Ma, W.M., Karbojian, A., Kudinov, P., Tran, C.T., Hansson, C.R., 2008. Ex-Vessel Corium Coolability and Steam Explosion Energetics in Nordic Light Water Reactors. Nordic Nuclear Safety Research, NKS-160, Sweden.
Hinds, W.C., 2012. Aerosol Technology: Properties, Behavior, and Measurement of Airborne Particles. John Wiley & Sons.
Hwang, G., Kaviany, M., Moriyama, K., Park, H.S., Hwang, B., Lee, M., Nasersharifi, Y., 2016. FARO tests corium-melt cooling in water pool: Roles of melt superheat and sintering in sediment. Nucl. Eng. Des. 305, 569–581.
Kaviany, M., 2011. Essentials of heat transfer: principles, materials, and applications. Cambridge University Press.
Kaviany, M., 2012. Principles of Heat Transfer in Porous Media. Springer Science & Business Media.
Khatib-Rahbar, M., Cazzoli, E., Lee, M., Nourbakhsh, H., Davis, R., Schmidt, E., 1989. A probabilistic approach to quantifying uncertainties in the progression of severe accidents. Nucl. Sci. Eng. 102 (3), 219–259.
Kim, J.T., Hong, S.W., Park, R.J., Kim, S.B., 2005. A study on the hydrogen behavior and its mitigation in the APR1400 containment during a severe accident (No. KAERI/TR–2948/2005). Korea Atomic Energy Research Institute.
Kim, W.K., Shim, J.H., Kaviany, M., 2017. Thermophysical properties of liquid UO_2, ZrO_2 and corium by molecular dynamics and predictive models. J. Nucl. Mater. 491, 126–137.
Kodur, V., 2014. Properties of Concrete at Elevated Temperatures. ISRN Civil Engineering.
Kudinov, P., Karbojian, A., Ma, W., Dinh, T.N., 2010. The DEFOR-S experimental study of debris formation with corium simulant materials. Nucl. Technol. 170 (1), 219–230.
Lee, M., Park, J. H., Kim, E., Park, H.S., 2016. Comparison of two phase pressure drop models in 1-D top flooded debris bed. In: Korean Nuclear Society 2016 Spring Meeting, Jeju.
Liu, C., Theofanous, T.G., 1995. Film boiling on spheres in single and two-phase flows: Part I. Experimental studies. In: Proc. ANS Nat. Heat Transfer Conf, August 1995, pp. 5–9.
Magallon, D., 2006. Characteristics of corium debris bed generated in large-scale fuel-coolant interaction experiments. Nucl. Eng. Des. 236 (19), 1998–2009.
Moriyama, K., Maruyama, Y., Usami, T., Nakamura, H., 2005. Coarse break-up of a stream of oxide and steel melt in a water pool (contract research). JAERI Res 2005-017.
Moriyama, K., Park, H.S., 2016. Simulation of melt jet breakup experiments by JASMINE with an empirical correlation for melt particle size distribution. J. Nucl. Sci. Technol. 53 (10), 1–14.
Moriyama, K., Park, H.S., Hwang, B., Jung, W.H., 2016a. Analysis of ex-vessel melt jet breakup and coolability. Part 1: Sensitivity on model parameters and accident conditions. Nucl. Eng. Des. 302, 107–117.
Moriyama, K., Park, H.S., Hwang, B., Jung, W.H., 2016b. Analysis of ex-vessel melt jet breakup and coolability. Part 2: uncertainty analysis. Nucl. Eng. Des. 302, 118–127.
Nukiyama, S., 1966. The maximum and minimum values of the heat Q transmitted from metal to boiling water under atmospheric pressure. Int. J. Heat Mass Transf. 9 (12), 1419–1433.
Park, J.H., Jeong, Y.H., Baek, W.P., Chang, S.H., 2001. An assessment methodology for in-vessel corium retention by external reactor vessel cooling during severe accidents in PWRs. Ann. Nucl. Energy 28 (12), 1237–1250.
Park, J., Kim, H., Hong, S., Ha, K., 2011. MCCI simulation for the APR-1400 TLOFW sequence. In: Trans. the Korean Nuclear Society 2011 Spring Meeting, May 2011.
Pohlner, G., Vujic, Z., Bürger, M., Lohnert, G., 2006. Simulation of melt jet breakup and debris bed formation in water pools with IKEJET/IKEMIX. Nucl. Eng. Des. 236 (19), 2026–2048.
Poulikakos, D., 1994. Conduction Heat Transfer. Prentice Hall.
Rempe, J.L., Lead, U.S., 2005. In-Vessel Retention Strategy for High Power Reactors.
Sairanen, R., Berthoud, G., Ratel, G., Meignen, R., Jacobs, H., Buerger, M., et al., 2007. OECD research programme on fuel-coolant interaction steam explosion resolution for nuclear applications-SERENA. Final Report-December 2006 (No. NEA-CSNI-R–2007-11). Organisation for Economic Co-Operation and Development.
Salikhov, T.P., Kan, V.V., Ronchi, C., 1999. Radiative properties of uranium dioxide near its melting point. Int. J. Thermophys. 20 (4), 1163–1176.
Schmidt, W., 2004. Influence of Multidimensionality and Interfacial Friction on the Coolability of Fragmented Corium.
Sehgal, B.R. (Ed.), 2011. Nuclear Safety in Light Water Reactors: Severe Accident Phenomenology. Academic Press.
Sevón, T., 2005. Molten Core-Concrete Interactions in Nuclear Accidents. Theory and Design of an Experimental Facility. VTT Research Notes, pp. 2311.
Schneider, P.J., 1985. Conduction Heat Transfer, Handbook of Heat Transfer Fundamentals. McGraw-Hill, New York.
Spencer, B.W., Wang, K., Blomquist, C.A., McUmber, L.M., Schneider, J.P., 1994. Fragmentation and Quench Behavior of Corium Melt Streams in Water (No. NUREG/CR–6133; ANL–93/32). Nuclear Regulatory Commission, Washington, DC (United States); Division of Systems Research, Argonne National Lab., IL (United States).
Todreas, N.E., Kazimi, M.S., 2012. Nuclear systems: thermal hydraulic fundamentals. CRC Press.
USNRC. SECY 93-087, 1993. Policy Technical and Licensing Issues Pertaining to Evolutionary and Advanced Light Water Reactor Design, April 2.
Voller, V., Cross, M., 1981. Accurate solutions of moving boundary problems using the enthalpy method. Int. J. Heat Mass Transf. 24 (3), 545–556.